SANDIA REPORT
SAND2020-9500
Printed September 2020

A Bézier Curve Informed Melt Pool Geometry to Model Additive Manufacturing Microstructures Using SPPARKS

Jeremy E. Trageser, John A. Mitchell

Prepared by
Sandia National Laboratories
Albuquerque, New Mexico 87185
Livermore, California 94550

Issued by Sandia National Laboratories, operated for the United States Department of Energy by National Technology & Engineering Solutions of Sandia, LLC.

Available to DOE and DOE contractors from

U.S. Department of Energy
Office of Scientific and Technical Information
P.O. Box 62
Oak Ridge, TN 37831

Telephone: (865) 576-8401
Facsimile: (865) 576-5728
E-Mail: reports@osti.gov
Online ordering: http://www.osti.gov/scitech

Available to the public from

U.S. Department of Commerce
National Technical Information Service
5301 Shawnee Road
Alexandria, VA 22312

Telephone: (800) 553-6847
Facsimile: (703) 605-6900
E-Mail: orders@ntis.gov
Online order: https://classic.ntis.gov/help/order-methods

ABSTRACT

Additive manufacturing is a transformative technology with the potential to manufacture designs which traditional subtractive machining methods cannot. Additive manufacturing offers fast builds at near final desired geometry; however, material properties and variability from part to part remain a challenge for certification and qualification of metallic components. AM induced metallic microstructures are spatially heterogeneous and highly process dependent. Engineering properties such as strength and toughness are significantly affected by microstructure morphologies resulting from the manufacturing process. Linking process parameters to microstructures and ultimately to the dynamic response of AM materials is critical to certifying and qualifying AM built parts and components and improving the performance of AM materials. The AM fabrication process is characterized by building parts layer by layer using a selective laser melt process guided by a computer. A laser selectively scans and melts metal according to a designated geometry. As the laser scans, metal melts, fuses, and solidifies forming the final geometry in a layerwise fashion. As the laser heat source moves away, the metal cools and solidifies forming metallic microstructures. This work describes a microstructure modeling application implemented in the SPPARKS kinetic Monte Carlo computational framework for simulating the resulting microstructures. The application uses Bézier curves and surfaces to model the melt pool surface and spatial temperature profile induced by moving the laser heat source; it simulates the melting and fusing of metal at the laser hot spot and microstructure formation and evolution when the laser moves away. The geometry of the melt pool is quite flexible and we explore effects of variances in model parameters on simulated microstructures.

ACKNOWLEDGMENT

The work in this report is part of a project focused on dynamic response of additively manufactured (AM) materials funded by the Advanced Certification and Qualification (ACQ) program. The authors gratefully acknowledge funding and support from the ACQ program and Paul Specht (org 01646) the project lead. The authors thank Dave Adams (org 01832) and Stan Pierce of Los Alamos National Laboratory for supplying microstructure images of AM and welded materials used to inspire and develop models described in this report.

CONTENTS

LIST OF FIGURES

LIST OF TABLES

NOMENCLATURE

Table 0-1.

Abbreviation	Definition
DOE	Department of Energy
HAZ	Heat Affected Zone
FZ	Fusion Zone
SPPARKS	Stochastic Parallel PARticle Kinetic Simulator
MCS	Monte Carlo Step

1. INTRODUCTION

Additive manufacturing is a transformative technology with the potential to offer unparalleled precision, flexibility, and speed in the manufacturing process. The fabrication process is characterized by the building of successive layers guided by a computer. While significant advances have been made which make additive manufacturing a potentially viable manufacturing technique for metals, there are few models which can accurately predict the underlying microstructure of the process. AM induced metallic microstructures are spatially heterogeneous and highly process dependent. Engineering properties such as strength and toughness are significantly effected by microstructure morphologies resulting from the manufacturing process. Linking process parameters to microstructures and ultimately to the dynamic response of AM materials is critical to certifying and qualifying AM built parts and components and improving the performance of AM materials.

This work aims to provide a model and computational simulation capability of metallic microstructure evolution which occurs during the additive manufacturing process. The work described herein builds upon the work in [9], and simulates melting, solidification, and microstructural evolution of material during the additive manufacturing process; it uses a modified Potts Monte Carlo method [2, 4] for simulation of grain growth which occurs during the additive manufacturing process. The model is available as an *app* in SPPARKS [6], an open-source kinetic Monte Carlo computational framework.

An outline of the work presented here is as follows. Technical details of the AM/Bézier application are described in Section 2, which is broken up into several subsections. In Section 2.1 we review the work of [9]. In Section 2.2 we look at the conversion between experimental parameters and SPPARKS parameters. In Section 2.3 we describe in detail the geometry of the melt pools implemented in the AM/Bézier application. Algorithms utilized in the AM/Bézier application are described in Section 2.4. Effects of model parameter variations on predicted microstructures are explored in Section 3. In particular, a description of the melt pool parameters is given in Section 3.1 which is then followed by Section 3.2 where numerical studies are presented and a variety of interesting properties of the parameters are deduced. Potential future work, closing remarks, and conclusions are given in Section 4.

2. METHODS

In this section, technical details of the additive manufacturing simulation model proposed in this work are described. The approach to simulating the additive manufacturing process is based on the framework introduced in [9]; this work is reviewed in Section 2.1. The contributions of the present work begins in Section 2.3 where a new melt pool geometry is described; this melt pool geometry framework is capable of describing a three-dimensional multilayered additive manufacturing process. The main algorithms implemented in the new SPPARKS AM/Bézier application are described in Section 2.4.

2.1. REVIEW

Consider a material domain on which the additive manufacturing process is to be simulated. Our goal is to simulate the additive manufacturing process wherein a heat source, frequently supplied by a laser, traverses the domain in order to induce melting followed by solidification. At any given moment, the domain is partitioned into four regions: a stationary region which is unaffected by the heat source, a heat affected zone (HAZ) which is a non-melted region where exposure to high temperatures induces changes in material properties, a fusion zone (FZ) where material has been melted by the heat source, and a melted region we refer to as the melt pool. In Figure 2-1 an illustration of the various regions is presented.

As in [9], we employ the Potts Monte Carlo model to simulate grain growth [5, 7, 8]. The Potts Monte Carlo model takes as input a temperature profile in terms of position and time. The temperature profile is determined by simulating the propagation of a weld pool through the material domain. The model begins with a discretization of the domain into spatial lattice sites. Each of these sites is identified with a particular grain by an identifier parameter referred to as spin. A region of contiguous sites which share a common spin is referred to as a grain. The grain boundary energy is the primary tool for determining grain growth and evolution. We define the grain boundary energy as the sum of all bonds between neighboring sites with dissimilar spins multiplied by the bond energy. Formally, the grain boundary energy is given by

$$E = \frac{J}{2}\sum_{i}^{N}\sum_{j}^{n}\left(1-\delta_{ij}\right), \tag{2.1}$$

where J represents the total bond energy, i is an index ranging over all N sites, and j is an index ranging over the n neighboring sites of i. The symbol δ_{ij} takes on a value of 1 when sites i and j have the same spin but is 0 otherwise; in this way grain boundary energy is accumulated in this sum.

Figure 2-1. Melt pool schematic: stationary region, melt pool, FZ, and HAZ.

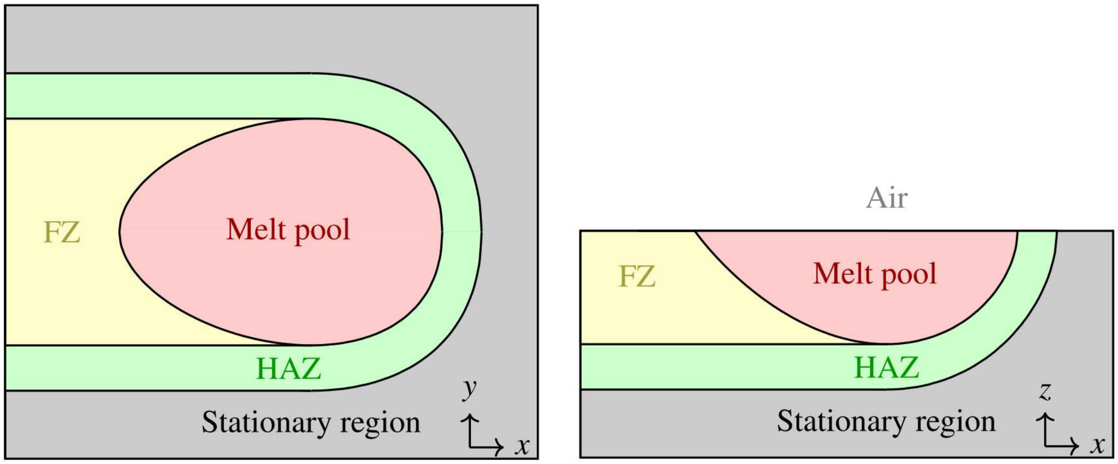

(a) *xy* **top view.** **(b)** *xz* **cross section.**

As in [9], we utilize the rejection kinetic Monte Carlo algorithm to simulate curvature driven grain growth. This is accomplished by attempting to change the spin of a site to the spin of a randomly selected dissimilar neighboring site. In determining whether to accept the change, we employ (2.1) to calculate the change in energy, ΔE, the resulting site change would produce. The probability P of a site changing its spin to that of the selected dissimilar neighboring site is then estimated by (*cf.* [3, 8, 5])

$$P = \begin{cases} M(T) & \Delta E \leq 0 \\ M(T)e^{-\frac{\Delta E}{kT}} & \Delta E > 0 \end{cases}, \tag{2.2}$$

where T is the temperature, k is the Boltzmann constant, and $M(T) \in [0,1]$ is referred to as the mobility and introduces temperature dependence into the model. If the temperature is sufficiently high so that $M(T)$ is near one, then from (2.2) we deduce changes to spin which reduce boundary energy are likely to take place while changes to spin which increase boundary energy are possible but less likely to occur. Figure 2-2 presents an example of this. On the other hand, if the temperature is sufficiently small so that $M(T)$ is small, then changes to spin are less likely to occur. While the melt pool is propagated through the medium, we suppose the temperature at a site, and consequently the mobility, is a function of the distance of the site from the melt pool surface. We further suppose mobility is zero for sites beyond a certain distance from the melt pool, which defines the boundary of the HAZ. While the model and its numerical implementation do not require a linear relationship, it is reasonable to assume the mobility at a lattice site $\mathbf{x}$ is defined by

$$M(\mathbf{x}) = \begin{cases} 1 - \frac{d(\mathbf{x})}{haz}, & d(\mathbf{x}) < haz \\ 0, & \text{else} \end{cases} \tag{2.3}$$

where $d(\mathbf{x})$ is the distance from the site $\mathbf{x}$ to the weld pool and haz is a constant which determines how far beyond the weld pool the HAZ extends. In Figure 2-3 we present illustrations of the

Figure 2-2. Example of grain evolution induced by (2.2). For sufficiently large mobility, the site labeled A is likely to change spin as this will result in a reduction of boundary energy of site A. On the other hand, site B is less likely to change its spin as this would result in an increase of boundary energy of site B.

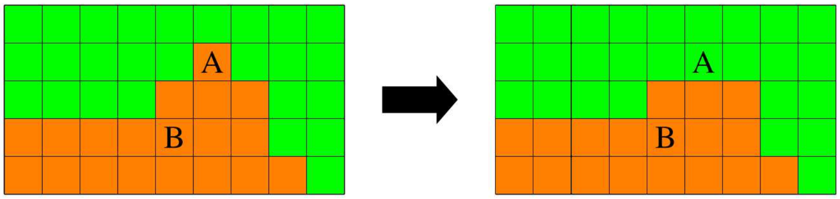

mobility profile for the melt pool geometry described by Case I Section 2.3.

The simulation of melting and solidification is accomplished as follows. A laser hot spot, represented by a melt pool, is propagated across and through the computational lattice. As the melt pool advances, sites entering the melt pool are assigned random spin values as they are assumed to be melted. Thus there is no inherent structure within the melt pool. As the melt pool continues to move, sites within the melt pool exit with no structure into the FZ and HAZ; these sites are not particularly special except for the fact they have no structure – they can become the site of a new grain or become part of another grain associated with a neighboring site – all determined by application of (2.2) with a mobility rule such as (2.3) when determining whether the spin of the site should be modified. The model has been implemented as an application, AM/Bézier, in SPPARKS, which is an open-sourced Sandia code which uses Monte Carlo methods to simulate microstructure evolution. As the spatial units are described by lattice points and time is described by Monte Carlo steps, in the next section we look at how to relate these quantities to experimental parameters.

2.2. RELATING SPPARKS PARAMETERS TO EXPERIMENTAL PARAMETERS

In the simulated AM process, advancement of time is accomplished by propagating a melt pool with speed v, where v is measured in lattice sites per Monte Carlo step (MCS). In order to inform our simulation with experimental conditions, we must relate simulation conditions such as time and distance to experimental conditions. The relationship between lattice sites and physical distance is accomplished by introducing a simulation lattice constant c, measured in microns per site, defined as the ratio of the experimentally measured melt pool width (in microns) to melt pool width (in sites). The following ratio is then used to relate simulation time (measured in MCS) to physical time

$$\gamma = c\frac{v}{V}, \tag{2.4}$$

Figure 2-3. Mobility determined by (2.3) for a prototype melt pool.

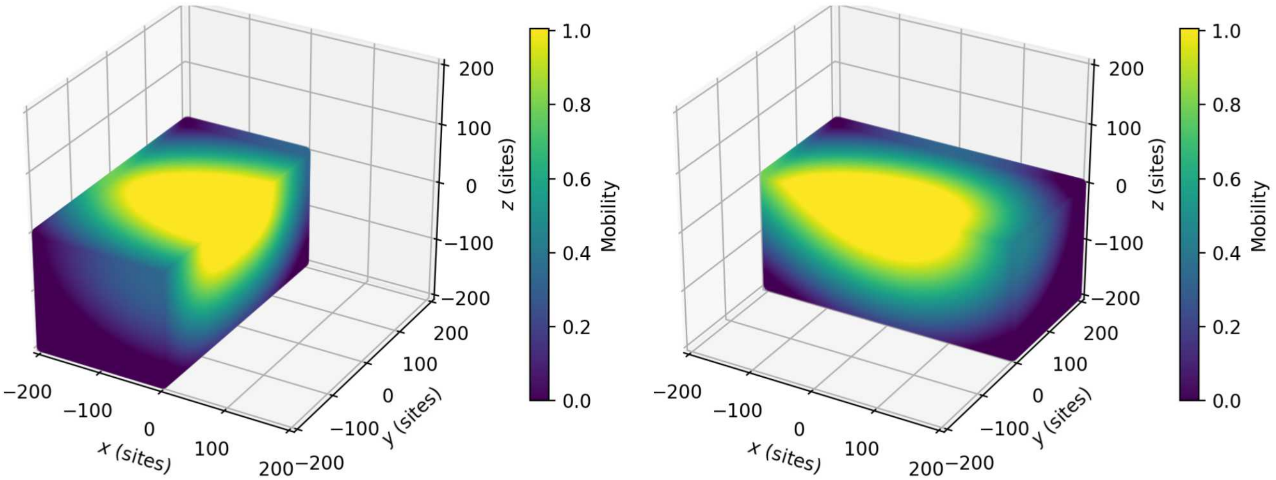

(a) Cut with $x = 0$ plane. **(b) Cut with $y = 0$ plane.**

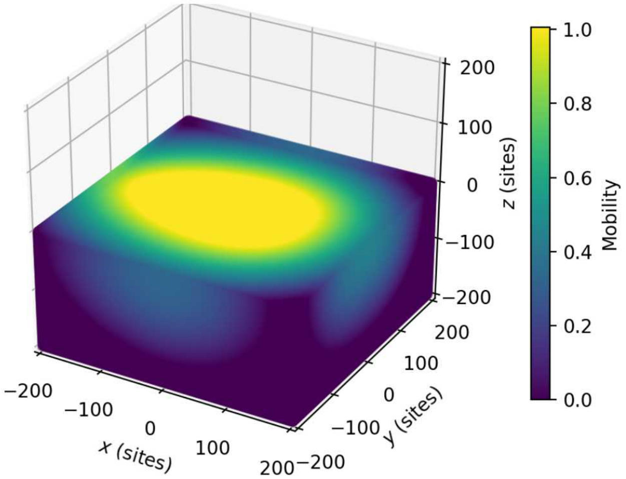

(c) Without a cutting plane.

where γ is a constant with units of seconds per MCS, and V is expressed in microns per second. Given the length scale parameter c, laser speed V, and an estimated simulation speed v, the parameter γ is calculated. The ideal value for v is one for which the model predicts a suitable microstructure. Generally this is unknown and v is only heuristically estimated. Using Equation (2.4), physical time t_p is related to simulation time t_s through the relationship $t_p = \gamma t_s$.

In the next section a novel melt pool geometry is introduced.

2.3. MELT POOL GEOMETRY

In this section we describe the parameterized geometry of the melt pool introduced in this work. Similar to [9], we employ a Bézier curve to describe the surface of the melt pool. The weld model [9] is intended for a single pass welding process where the heat source fully penetrates the plate thickness; hence the melt pool surface is defined by the flat bottom surface of the welded plate and the melt pool sidewalls. In contrast, the work herein focuses on a multi-layer additive manufacturing process where the heat source introduces a fully three-dimensional melt pool geometry with a bottom surface not defined by the bottom of a plate. This is accomplished by introducing a second Bézier curve describing the spine of the melt pool and formulating a surface as a function of the spine and surface boundary curves. Before formally describing the geometry of the melt pool, we begin with a short introduction to Bézier curves.

Bézier curves are parametric curves frequently employed in computer graphics. The Bernstein polynomials serve as a basis for Bézier curves and are regularly employed to describe them. The Bernstein polynomials of degree n are defined by

$$B_{i,n}(u) := \frac{n!}{i!(n-i)!} u^i (1-u)^{n-i}, \quad i \in [0,1,\ldots,n], \quad u \in [0,1]. \tag{2.5}$$

The Bézier curve in dimension d of degree n may then be defined by

$$\mathbf{C}(u) := \sum_{i=0}^{n} \mathbf{P}_i B_{i,n}(u), \quad u \in [0,1], \tag{2.6}$$

where $\{\mathbf{P}_i\} \in \mathbb{R}^d$ are referred to as control points. The melt pool geometry in this work is entirely determined by a scaling term $\mathbf{a}$ and two Bézier curves; specifically, a degree four Bézier curve

$$\mathbf{C}^t(u) := \sum_{i=0}^{4} \mathbf{P}_i B_{i,4}(u), \quad u \in [0,1], \tag{2.7}$$

describing half the surface boundary of the melt pool (*e.g.* Figure 2-4a) and a degree four Bézier curve

$$\mathbf{C}^b(u) := \sum_{i=0}^{4} \mathbf{Q}_i B_{i,4}(u), \quad u \in [0,1], \tag{2.8}$$

describing the spine of the melt pool (*e.g.* Figure 2-4b). With $\mathbf{C}^t(u)$ and $\mathbf{C}^b(u)$, we formulate a surface as a degree three Bézier curve $\mathbf{S}(u,v)$, where the control points are functions of $\mathbf{C}^t(u)$ and $\mathbf{C}^b(u)$:

$$\mathbf{S}(u,v) := \sum_{i=0}^{3} \mathbf{R}_i(u) B_{i,3}(v), \quad u \in [0,1], \quad v \in [0,1], \tag{2.9}$$

where

$$\begin{aligned} R_0(u) &= \mathbf{C}^t(u), & R_1(u) &= \mathbf{C}^t(u) + \tfrac{1}{2}\begin{bmatrix} 0 \\ 0 \\ C_3^b(u) \end{bmatrix}, \\ R_2(u) &= \mathbf{C}^t(u) + \begin{bmatrix} 0 \\ 0 \\ C_3^b(u) \end{bmatrix}, & R_3(u) &= \mathbf{C}^b(u). \end{aligned} \tag{2.10}$$

In (2.10) we use $C_3^b(u)$ to refer to the third component of $\mathbf{C}^b(u)$. A well-known property of Bézier curves implies $\mathbf{S}(u,0) = \mathbf{C}^t(u)$ and $\mathbf{S}(u,1) = \mathbf{C}^b(u)$ so the pool surface boundary and spine are exactly represented in $\mathbf{S}(u,v)$. In order to provide flexibility when calibrating with experimentally determined parameters, we allow the various components of the surface to be scaled. The final formulation for the boundary of our melt pool is determined by the surface

$$\mathbf{S}^{\mathbf{a}}(u,v) := \begin{bmatrix} a_1 S_1(u,v) \\ a_2 S_2(u,v) \\ a_3 S_3(u,v) \end{bmatrix}, \tag{2.11}$$

where $\mathbf{a} \in \mathbb{R}^3$ is used for scaling and S_1, S_2, and S_3 are the three components of $\mathbf{S}$. Since $\mathbf{C}^t(u)$ only describes half of the surface boundary, $\mathbf{S}^{\mathbf{a}}(u,v)$ only describes half of the melt pool surface. The full surface is determined by reflecting $\mathbf{S}^{\mathbf{a}}(u,v)$ across a plane which is orientation specific. In this work the surfaces will be oriented so that the reflection is across the xz plane. For example, in Figure 2-5 are representative plots of the spine and surface boundaries of three melt pools. Taking the corresponding surface $\mathbf{S}(u,v)$ and its reflection across the xz plane produces the melt pool surfaces presented in Figure 2-6.

To enforce this orientation on our melt pool geometries, we impose several restrictions. For convenience, we employ the notation P_{i_j} to refer to the j^{th} component of control point $\mathbf{P}_i$. On the pool surface boundary control points $\{\mathbf{P}_i\}$ we impose

$$P_{i_3} = 0, \quad i = 1, \ldots, 4, \tag{2.12}$$

so that the curve $\mathbf{C}^t(u)$ lies in the $z = 0$ plane. In addition, we require

$$P_{0_2} = P_{4_2} = 0 \text{ and } P_{i_2} > 0, \quad i = 1,2,3, \tag{2.13}$$

so that $\mathbf{C}^t(u)$ has endpoints on the x axis and is contained in the $y \geq 0$ region of the $z = 0$ plane; see Figure 2-4a for an example demonstrating these constraints. In order to provide a smooth transition (in the sense of derivatives) from the region $y \geq 0$ to $y \leq 0$ under reflection, we impose

$$P_{0_1} = P_{1_1} \text{ and } P_{3_1} = P_{4_1}. \tag{2.14}$$

Lastly, from (2.12) and (2.13) we see the second components of $\mathbf{P}_1, \mathbf{P}_2$, and $\mathbf{P}_3$ determine the width of the melt pool; we select these terms so that the maximum distance between the curve $\mathbf{C}^t(u)$ and the x-axis is normalized to unity. This permits us to easily prescribe the width and length of the melt pool with the scaling parameter $\mathbf{a}$. Specifically, the width of the melt pool described by $\mathbf{S}^{\mathbf{a}}(u,v)$ is $2a_2$ while the length is $a_1\left|P_{4_1} - P_{0_1}\right|$. See Figures 2-4a, 2-4c, and 2-4e for some example cases of the surface boundary curve $\mathbf{C}^t(u)$.

Similarly, on the melt pool spine control points $\{\mathbf{Q}_i\}$ we impose

$$Q_{i_2} = 0, \quad i = 1, \ldots, 4 \tag{2.15}$$

so curve $\mathbf{C}^b(u)$ lies in the $y = 0$ plane. In addition, to provide realistic derivatives at the endpoints of the curve $\mathbf{C}^b(u)$ we impose

$$Q_{3_1} = Q_{4_1} \text{ and } \mathbf{Q}_0 = \mathbf{Q}_1. \tag{2.16}$$

The main motivation for selecting four control points for $\mathbf{C}^b(u)$ is to impose the condition

$$P_{i_1} = Q_{i_1}, \quad i = 1, \ldots, 4, \tag{2.17}$$

which provides the convenient property that the first component of $\mathbf{S}^{\mathbf{a}}(u,v)$ is independent of v. This can be seen by imposing (2.17) on (2.9) and noting that Bernstein polynomials of degree n form a partition of unity. Lastly, from (2.15) and (2.16) we see the third components of $\mathbf{Q}_2$ and $\mathbf{Q}_3$ dictate melt pool depth; these terms are selected so that the maximum distance between the curve $\mathbf{C}^b(u)$ and the x-axis is normalized to unity. This permits us to easily prescribe the depth of the melt pool with the scaling parameter $\mathbf{a}$; the melt pool depth of $\mathbf{S}^{\mathbf{a}}(u,v)$ is a_3. See Figures 2-4b, 2-4d, and 2-4f for examples of the spine curve $\mathbf{C}^b(u)$.

From these above constraints, the melt pool geometry determined by $\mathbf{S}^{\mathbf{a}}(u,v)$ inherits several properties which are summarized below:

1. The length, width, and depth of the melt pool are $a_1\left|P_{4_1} - P_{0_1}\right|$, $2a_2$, and a_3 respectively.
2. The first component of $\mathbf{S}^{\mathbf{a}}(u,v)$ is independent of v.
3. Melt pool surface $\mathbf{S}(u,v)$ exactly fits Bézier specified spine and top surface curves defined in Equations (2.7) and (2.8). Specifically, $\mathbf{S}(u,0) = \mathbf{C}^t(u)$ and $\mathbf{S}(u,1) = \mathbf{C}^b(u)$;
4. The melt pool surface $\mathbf{S}^{\mathbf{a}}(u,v)$ is smooth in the sense of differentiability.
5. The full melt pool surface is described by $\mathbf{S}^{\mathbf{a}}(u,v)$ and its reflection across $y = 0$ plane.

There is a significant degree of flexibility in describing the melt pool geometry through a selection of control points – even after the above constraints are applied. Three different melt pool geometries are numerically explored in Section 3.1.

Figure 2-4. Plots of Bézier curves describing the top surface and spine boundary of the melt pool along with their corresponding control points for Cases I, II, and III.

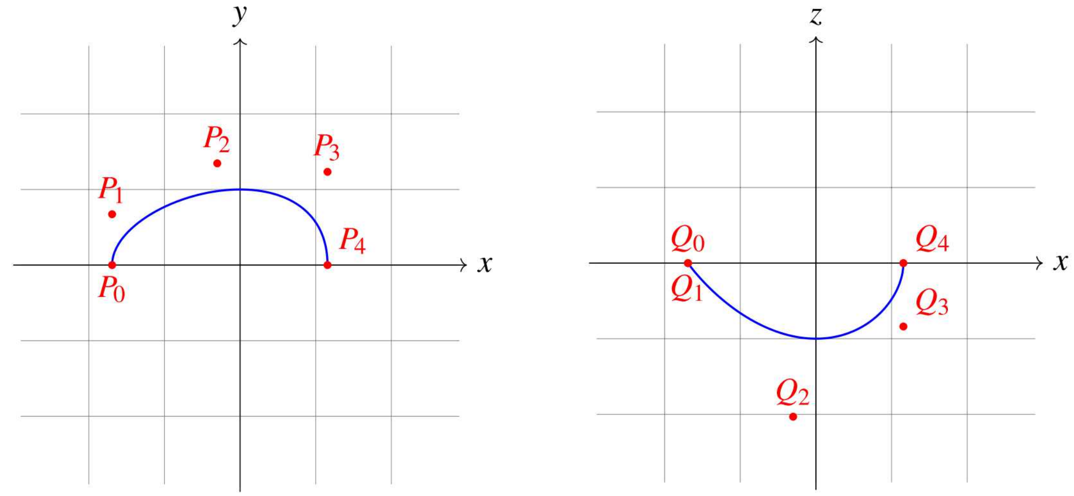

(a) Case I Surface Boundary **(b) Case I Spine Boundary**

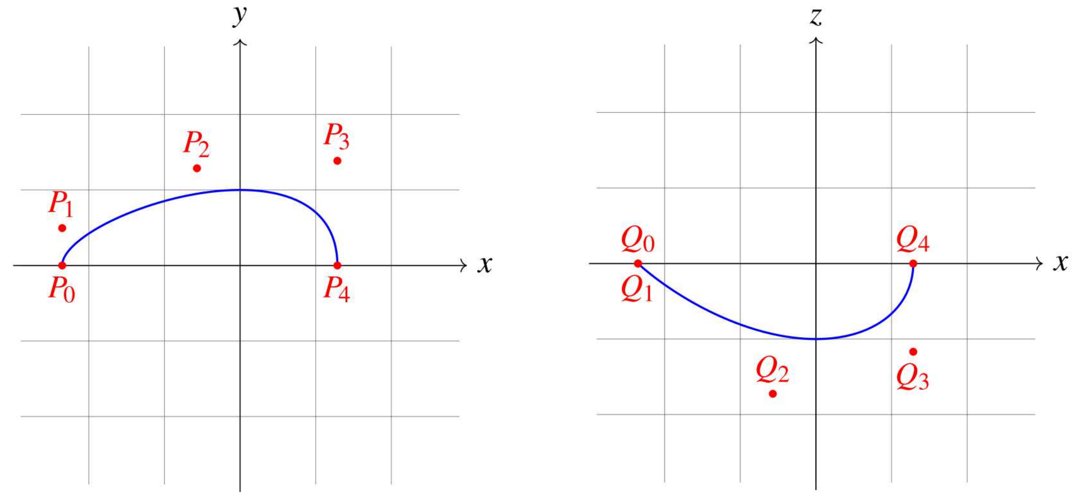

(c) Case II Surface Boundary **(d) Case II Spine Boundary**

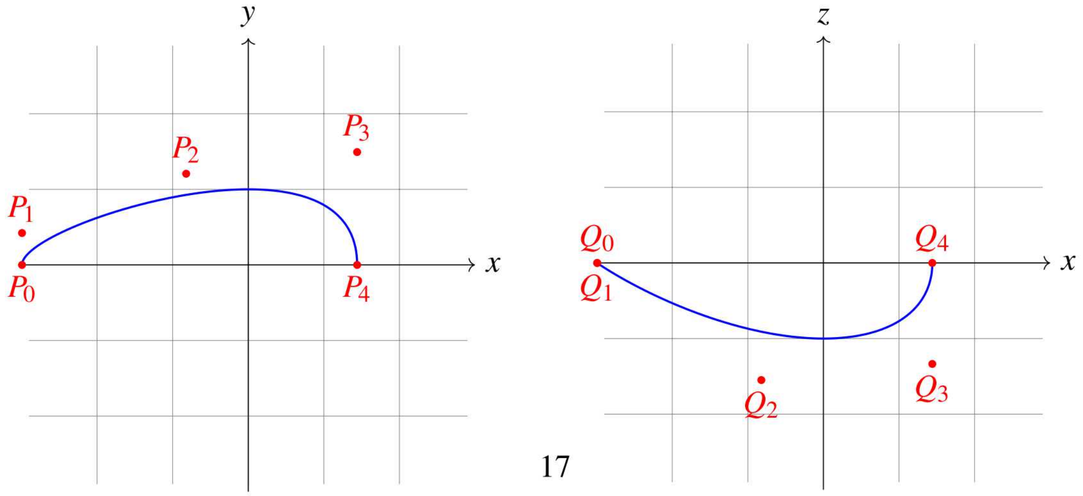

(e) Case III Surface Boundary **(f) Case III Spine Boundary**

Figure 2-5. Various yz cross sections of the melt pool boundary for Cases I, II, and III.

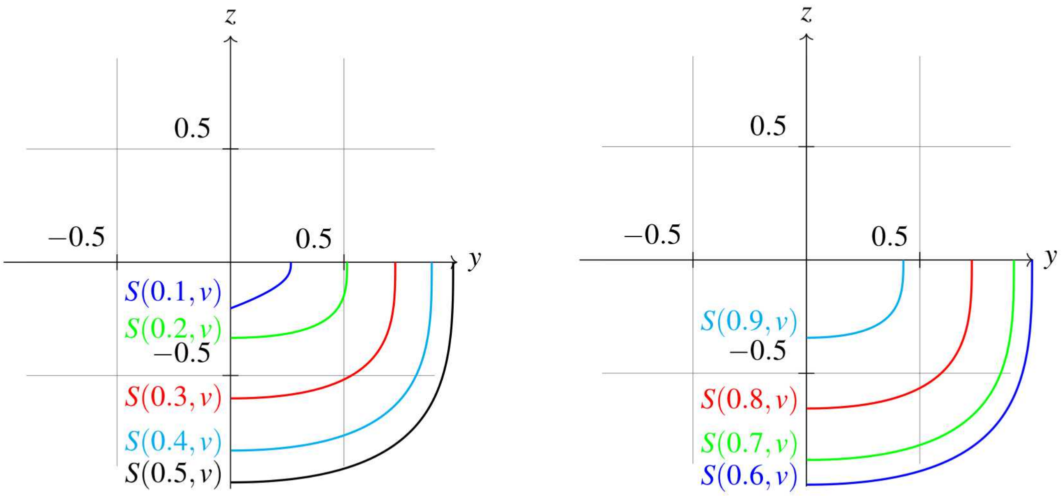

(a) Case I: $\mathbf{u} = \mathbf{0.1}, \mathbf{0.2}, \mathbf{0.3}, \mathbf{0.4}, \mathbf{0.5}$.

(b) Case I: $\mathbf{u} = \mathbf{0.6}, \mathbf{0.7}, \mathbf{0.8}, \mathbf{0.9}$.

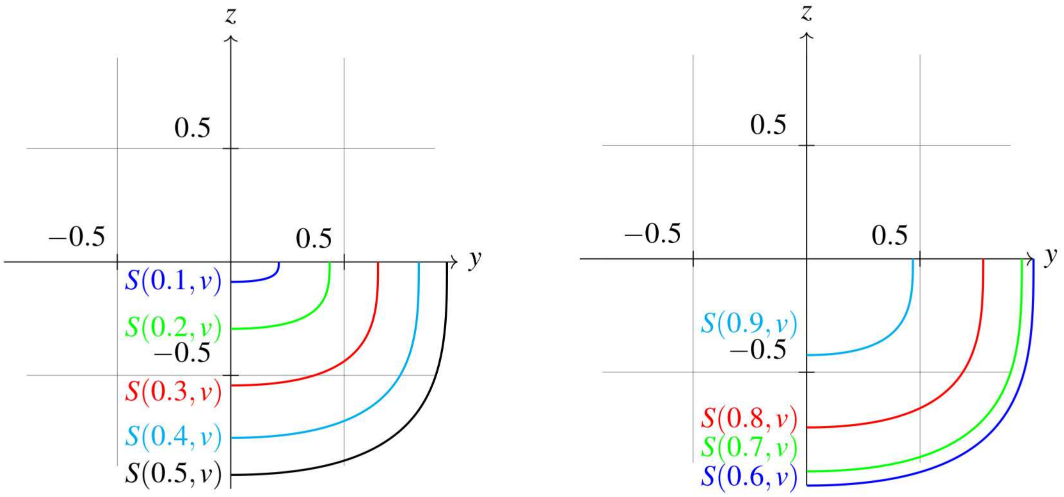

(c) Case II: $\mathbf{u} = \mathbf{0.1}, \mathbf{0.2}, \mathbf{0.3}, \mathbf{0.4}, \mathbf{0.5}$.

(d) Case II: $\mathbf{u} = \mathbf{0.6}, \mathbf{0.7}, \mathbf{0.8}, \mathbf{0.9}$.

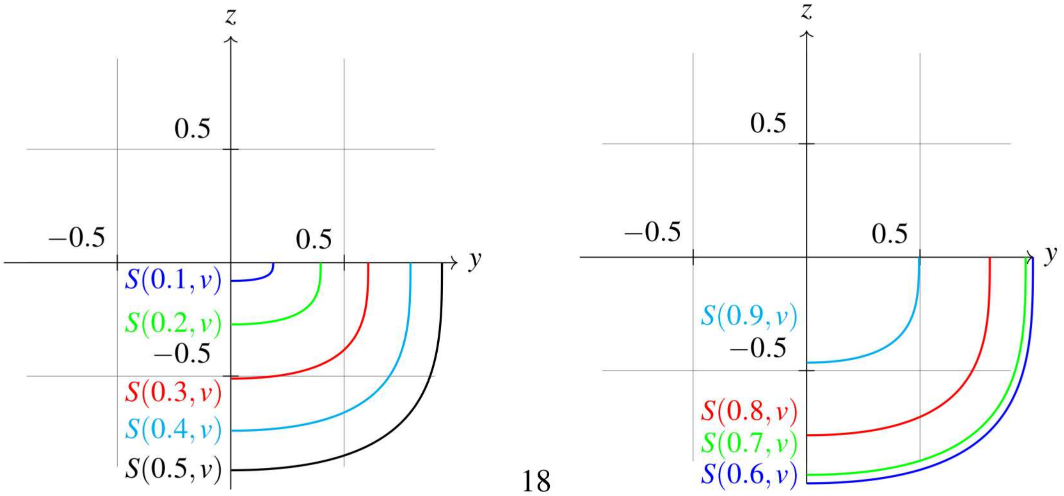

(e) Case III: $\mathbf{u} = \mathbf{0.1}, \mathbf{0.2}, \mathbf{0.3}, \mathbf{0.4}, \mathbf{0.5}$.

(f) Case III: $\mathbf{u} = \mathbf{0.6}, \mathbf{0.7}, \mathbf{0.8}, \mathbf{0.9}$.

Figure 2-6. Three dimensional plots of melt pool boundaries.

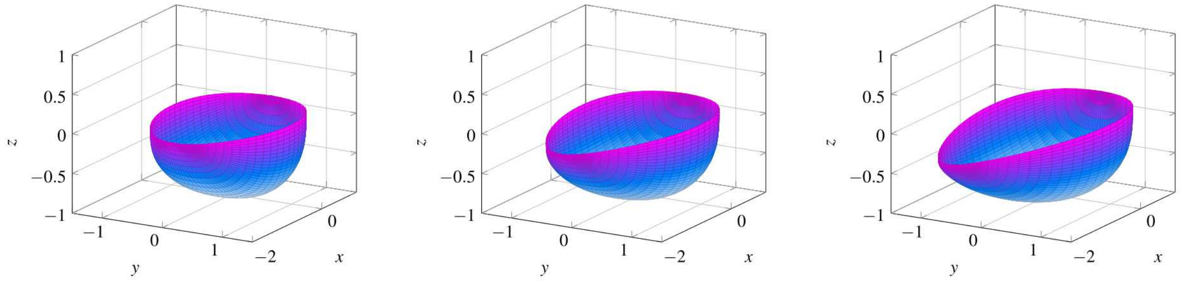

(a) Case I (b) Case II (c) Case III

2.4. DETERMINING THE MOBILITY OF SITES

In this section we discuss the process of calculating the mobility. Recall from (2.3) that to calculate mobility at a site, we need to calculate the distance from the site to the melt pool surface. We accomplish this in two steps. The first step is to determine whether the site $\mathbf{x}$ is inside (distance is zero) or outside the melt pool. If the point is outside the melt pool then we calculate the distance to the melt pool surface. By symmetry we only need to consider the $y \geq 0$ region of our space. To see this note any site in the region $y < 0$ has the same distance from the melt pool surface as its reflection across the $y = 0$ plane.

2.4.1. Determining whether a site lies outside the melt pool

Algorithm 1 describes the method implemented in AM/Bézier for determining whether a site $\mathbf{x} := \langle x_1, x_2, x_3 \rangle$ is outside the melt pool. Recall the melt pool boundary is described by $S^{\mathbf{a}}(u,v)$ and its reflection across the $y = 0$ plane. Due to this symmetry, the algorithm is designed for sites in the half space defined by $y \geq 0$, and we merely reflect sites with component $x_2 \leq 0$ across the $y = 0$ plane when determining whether the site is outside the melt pool. By construction (see Section 2.3), the surface $\mathbf{S}^{\mathbf{a}}(u,v)$ is independent of v in its first component and thus we may solve (e.g. with Newton's method)

$$x_1 = S^{\mathbf{a}}_1(u^*)$$

for u^*. Then $\mathbf{S}^{\mathbf{a}}(u^*,v)$ for $v \in [0,1]$ is the curve on the $y \geq 0$ melt pool boundary which has the same first component as $\mathbf{x}$. Next, we find the value v^* which solves (e.g. with Newton's method)

$$x_3 = S^{\mathbf{a}}_3(u^*,v^*).$$

Then $\mathbf{S}^{\mathbf{a}}(u^*,v^*)$ is the unique point on the $y \geq 0$ melt pool boundary having the same first and third components as the site $\mathbf{x}$. We simply compare the second components, i.e. $|x_2| < S^{\mathbf{a}}_2(u^*,v^*)$, to determine whether the site is inside the melt pool. A schematic of this algorithm is shown in Figure 2-7.

Figure 2-7. Visualization of Algorithm 1. The blue curve denotes the set of points on $S^{\mathbf{a}}(u^*,v)$ with the same first component as $\mathbf{p}$. The black arrow denotes the unique point on the blue curve where $\mathbf{S}^{\mathbf{a}}(u^*,v^*)$ has the same third component as $\mathbf{p}$. The final inside/outside test is conducted on the second component of $\mathbf{p}$ and $\mathbf{S}^{\mathbf{a}}(u^*,v^*)$.

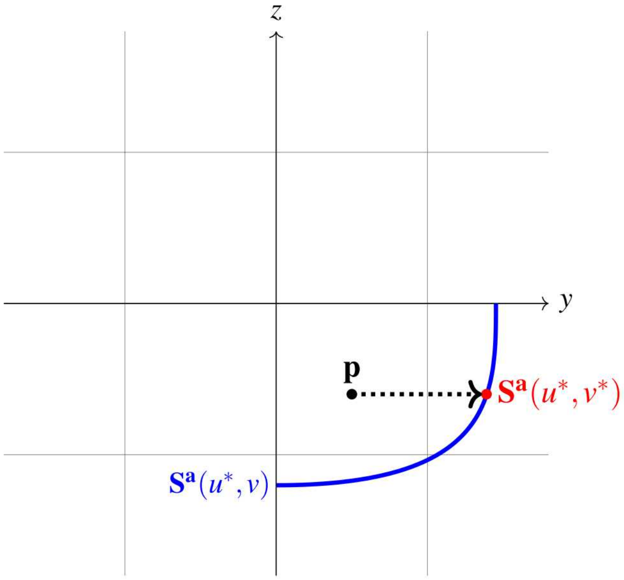

Algorithm 1 Inside or Outside the Melt Pool

```
procedure InsideOutside($\mathbf{x},\mathbf{a},\mathbf{P}_i,\mathbf{Q}_i$)
    bool inside = FALSE.
    if ($P_{0_1} \leq x_1 \leq P_{4_1}$) and ($|x_2| \leq a_2$) and ($x_3 \geq -a_3$) then    ▷ Bounding box around pool.
        Solve for $u^*$ in $S_1^{\mathbf{a}}(u^*) = x_1$.    ▷ $S_1^{\mathbf{a}}(u,v)$ is constant in $v$.
        if $a_3 R_{3_3}(u^*) \leq z \leq a_3 R_{0_3}(u^*)$ then
            Solve for $v^*$ in $S_3^{\mathbf{a}}(u^*,v^*) = x_3$.
            if $|x_2| \leq S_2^{\mathbf{a}}(u^*,v^*)$ then inside = TRUE
    return inside
```

2.4.2. Determining the distance from a site to the melt pool

Algorithm 2 describes the method implemented in AM/Bézier for determining the distance from a site $\mathbf{x}$ to the melt pool surface described by $\mathbf{S^a}(u,v)$. The Euclidean distance from the site $\mathbf{x}$ to the surface $\mathbf{S^a}(u,v)$ is given by

$$d(\mathbf{S^a}(u,v),\mathbf{x}) := \min_{u,v} \|\mathbf{S^a}(u,v)-\mathbf{x}\| = \min_{u,v} \sqrt{(\mathbf{S^a}(u,v)-\mathbf{x})\cdot(\mathbf{S^a}(u,v)-\mathbf{x})}. \tag{2.18}$$

Rather than minimizing (2.18) directly, we minimize $d^2(\mathbf{S^a}(u,v),\mathbf{x})$ which equivalently has a minimum when (2.18) does. Newton's method can be utilized for this purpose. To that end, we find the arguments u and v corresponding to the minimum distance through iterations of

$$\begin{bmatrix} u_{n+1} \\ v_{n+1} \end{bmatrix} = \begin{bmatrix} u_n \\ v_n \end{bmatrix} - J^{-1}(u_n,v_n)\nabla d^2(\mathbf{S^a}(u,v),\mathbf{x}), \tag{2.19}$$

where J is the Hessian of $d^2(\mathbf{S^a}(u,v),\mathbf{x})$ and ∇ is the gradient operator. In order to provide a reasonable initial guess for Newton's method, we employ a k-d tree created from points on the surface $\mathbf{S^a}(u,v)$. To create the tree, we first select a sampling from the region $[0,1]\times[0,1]$. We found that a non uniform sampling with points concentrated near the boundaries of the square $[0,1]\times[0,1]$ was more efficient. The k-d tree is then generated from the image of the sampling under $\mathbf{S^a}(u,v)$. We have summarized the algorithm for finding the distance from site $\mathbf{x}$ to the melt pool in Algorithm 2.

Algorithm 2 Distance to the Meltpool

```
procedure DistanceToMeltPool($\mathbf{x}, \mathbf{a}, \mathbf{P}_i, \mathbf{Q}_i$, KDTree, tolerance)
    Query KDTree for initial guess $(u,v)$.
    while tolerance < residual do
        set $\begin{bmatrix} u \\ v \end{bmatrix} = \begin{bmatrix} u \\ v \end{bmatrix} - J^{-1}(u,v)\nabla d^2(\mathbf{S^a}(u,v),\mathbf{x})$.
        set residual = $\|\nabla d(\mathbf{S^a}(u,v),\mathbf{x})\|$.
    return $d(\mathbf{S^a}(u,v),\mathbf{x})$.
```

3. PARAMETER STUDY

This section explores model parameters and their impact on simulated microstructures. In an attempt to reproduce experimental results, we adopt material parameters from experiments presented in [1]. Our numerical experiments correspond to a manufactured material with dimensions 10mm×10mm×7.62mm as seen in Figure 3-1. This is considerably smaller than material samples constructed [1] for mechanical evaluation; however, microstructure images taken [1] are of a similar size and consequently for comparative purpose these dimensions are sufficient.

In [1], each fused layer of the manufacturing process increased the height (z dimension) of the material by 1.27mm. In addition, they implemented a parallel scan path with hatch spacing (distance between parallel scan lines) of 1.925mm, where each layer is constructed with an identical scan pattern. A single layer of this process is presented in Figure 3-2 where scan lines are anti-parallel on a layer. The melt pool width was recorded as 4mm. To convert these parameters to SPPARKS parameters, we assume a lattice constant $c = 20\ \mu$m/site (*cf.* (2.4)). We have summarized experimental parameters along with corresponding SPPARKS counterparts in Table 3-1. All simulations used a simulation temperature $kT = 0.25$ and a random initialization of all lattice site spin values; site spin values were assigned using the same random seed for all experiments to facilitate parameter comparisons.

Table 3-1. Build parameters for additive manufacturing.

Parameter	Experimental	SPPARKS
Pool width	4mm	200 sites
Layer dimensions	10mm×10mm	500 sites×500 sites
Layer thickness	1.27mm	64 sites
Hatch spacing	1.925mm	96 sites

3.1. MELT POOL PARAMETERS

Melt pool surface geometries developed in this study are inspired by laboratory weld studies on molybdenum [10]. On the left side of Figure 3-3 are images of three melt pool surface geometries generated experimentally [10]. On the right side of Figure 3-3 are three Bézier curve

Figure 3-1. Dimensions of simulated AM material.

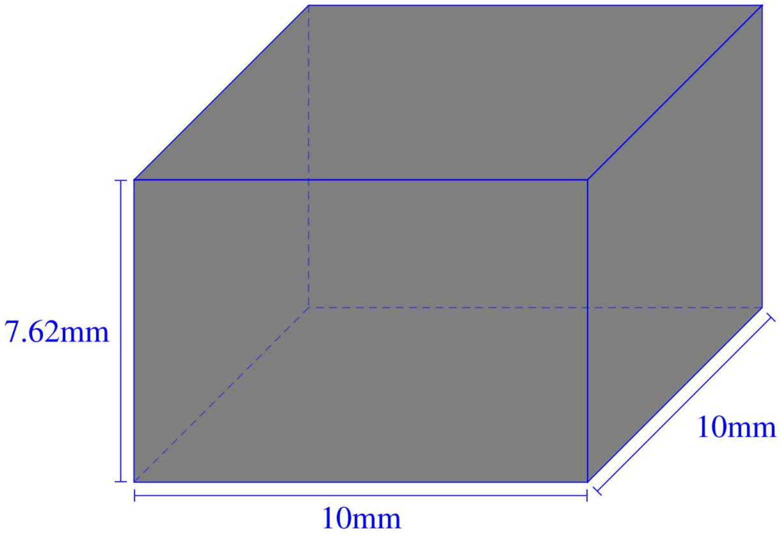

Figure 3-2. Parallel scan path schematic.

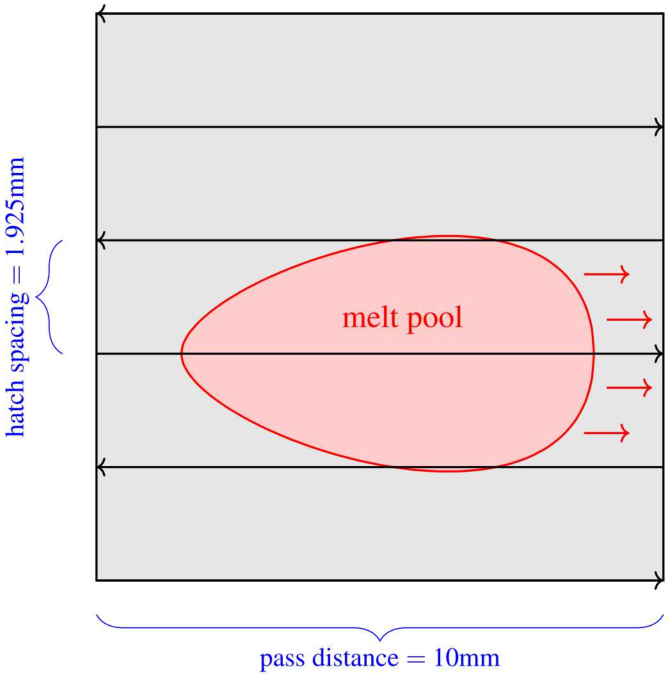

Figure 3-3. Experimental melt pool shapes (left) [10] and $S(u,0)$ for Cases I, II, and III (right). Melt pool width for all three cases, 2.54 mm.

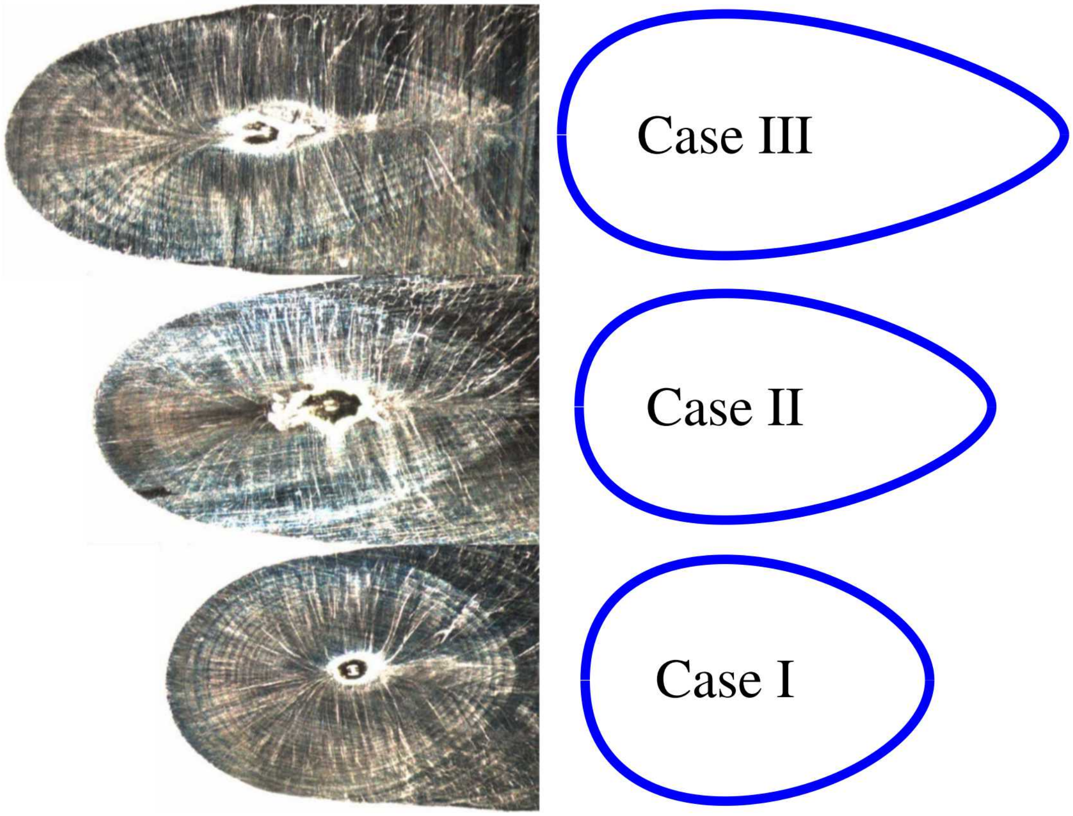

approximations, labeled Cases I, II, and III, to experimental melt pool geometries. The variation in experimental pool geometries was a consequence of adjustments to weld speed and power while attempting to hold pool width constant at 2.54mm. In particular, experimental weld speeds utilized were $8.47, 10.58$, and 12.7 m/s for Cases I, II, and III respectively. The control point parameters which generated the approximations are summarized in Table 3-2a. In addition, in Figures 2-4a, 2-4c, and 2-4e, the corresponding Bézier curves are plotted with their corresponding control points from Table 3-2a.

The melt pool subsurface is generally more difficult to determine from experiments as it is not visible in images such as those shown in Figure 3-3; moreover, these images are weld images where the melt pool spine does not even exist. Given in 3-2b are three plausible sets of control points selected for the curve describing the spine. Plots of control points and corresponding Bézier curves are shown in Figures 2-4b, 2-4d, and 2-4f.

To provide a better intuition on the full melt pool geometry, in Figures 2-5a, 2-5b, 2-5c, 2-5d, 2-5e, and 2-5f are plots of the yz cross sections of the melt pools for Cases I, II, and III respectively. Lastly, in Figure 2-6 we provide a full three-dimensional plot of the melt pool boundary for the three cases. Currently, the only melt pool geometries implemented into the AM/Bézier application of SPPARKS are Cases I, II, and III. Implementing additional geometries

Table 3-2. Control points for the Bézier curves describing the spine and surface boundary of the melt pool.

Case I	x	y	z
P_0	-1.69187	0.00000	0.00000
P_1	-1.69187	0.67283	0.00000
P_2	-0.30135	1.34567	0.00000
P_3	1.15656	1.23353	0.00000
P_4	1.15656	0.00000	0.00000
Case II	**x**	**y**	**z**
P_0	-2.35192	0.00000	0.00000
P_1	-2.35192	0.49508	0.00000
P_2	-0.56962	1.28722	0.00000
P_3	1.28695	1.38624	0.00000
P_4	1.28695	0.00000	0.00000
Case III	**x**	**y**	**z**
P_0	-2.99272	0.00000	0.00000
P_1	-2.99272	0.42221	0.00000
P_2	-0.82137	1.20631	0.00000
P_3	1.44046	1.49281	0.00000
P_4	1.44046	0.00000	0.00000

(a) Control points for the Bézier curves describing the surface of the melt pool.

Case I	x	y	z
Q_0	-1.69187	0.00000	0.00000
Q_1	-1.69187	0.00000	0.00000
Q_2	-0.30135	0.00000	-2.03387
Q_3	1.15656	0.00000	-0.83758
Q_4	1.15656	0.00000	0.00000
Case II	**x**	**y**	**z**
Q_0	-2.35192	0.00000	0.00000
Q_1	-2.35192	0.00000	0.00000
Q_2	-0.56962	0.00000	-1.72494
Q_3	1.28695	0.00000	-1.16855
Q_4	1.28695	0.00000	0.00000
Case III	**x**	**y**	**z**
Q_0	-2.99272	0.00000	0.00000
Q_1	-2.99272	0.00000	0.00000
Q_2	-0.82137	0.00000	-1.54935
Q_3	1.44046	0.00000	-1.33602
Q_4	1.44046	0.00000	0.00000

(b) Control points for the Bézier curves describing the spine of the melt pool.

is planned for a future release. Nonetheless, these three geometries may be used to generate a large variety of shapes using different width to depth aspect ratios.

In addition to the melt pool geometries Cases I, II and III, there are a variety of other melt pool parameters implemented in AM/Bézier which affect generated microstructures. The scaling term $\mathbf{a}$ (see (2.11)) determines melt pool length, width, and depth. The parameter haz from (2.3) determines the mobility profile outside the melt pool. Lastly, weld speed v_p is a key parameter which significantly alters microstructures. We have compiled the currently implemented parameters of AM/Bézier in Table 3-3. In addition, in Figures 3-4a and 3-4b are illustrations for some parameters. In Section 3.2 we detail our exploration of parameter variations on generated microstructures.

3.2. PARAMETER EXPERIMENTS

For parameter experiments we explore variations in generated microstructures with a focus on the AM/Bézier model parameters summarized in Table 3-3. In particular, we investigate variances of weld pool geometry (Case I, II, or III), the size of HAZ using parameter haz, simulation laser

Table 3-3. Melt pool parameters for the SPPARKS AM/Bézier application.

Parameter	Description
shape	Determines melt pool shape, either Case I, II, or III.
haz > 0	Size of the HAZ in sites.
$v_p > 0$	Weld speed expressed in sites per MCS.
a_1	Melt pool length divided by $\|P_{4_1} - P_{0_1}\|$ expressed in sites.
a_2	Half melt pool width expressed in sites.
a_3	Melt pool depth expressed in sites.

speed v_p, and melt pool depth a_3. Since we have experimental data for melt pool width (*cf.* Table 3-1), we do not consider variations in a_2; melt pool length follows from pool geometry (Case I, II or III) once pool width is specified. If a_1 is allowed to change, then pool geometry would not conform to the melt pool shapes I, II or III. However, performing experiments on shapes I, II, III does allow us to observe effects due to changes in melt pool length. Thus, we do not vary a_1 and instead preserve the melt pool aspect ratio of width to length implied by pool shapes I, II and III shown in Figure 3-3.

We begin with the nominal set of parameters given in Table 3-4. Layers of thickness 64 sites are added one at a time as the build proceeds. Melt pool depth is generally greater than layer thickness; to fuse adjacent layers together, a nominal melt pool depth of $a_3 = 80$ sites was selected. For every experiment we visualize planar cuts of the microstructure at: $x = 250$, $y = 250$, $z = 1$, and $z = 64$. The build plane and bottom of the first layer $z = 1$ is included for comparison purposes. The top of the first layer is visualized for a cut at $z = 64$. It is interesting to observe effect of fusing one layer to the adjacent layer just below. At $z = 64$ two images are presented: 1) just after the first layer has been built but prior to the start of the second layer – labeled as first pass; 2) just after the second layer build has fused onto the first layer – labeled as second pass. The cases $x = 250$ (X-cut) and $y = 250$ (Y-cut) illustrate microstructure development in the vertical direction and are a combination of multiple layers in the build process. The haz parameter defines a distance perpendicular to the melt pool surface where microstructure evolution occurs – this region is where mobility is computed; haz is a length scale parameter which defines the region over which effects of temperature influence microstructure. The nominal base case microstructures, shown in Figure 3-5, are used for comparison purposes with microstructures generated by isolating and varying parameters from Table 3-3.

3.2.1. Variances in the melt pool shape

In this section, effects of changing melt pool shape are explored; the nominal shape is case II per Table 3-4. Shown in Figures 3-6 and 3-7 are snapshots of microstructures generated for cases I

Figure 3-4. SPPARKS AM/Bézier application melt pool parameters illustrated.

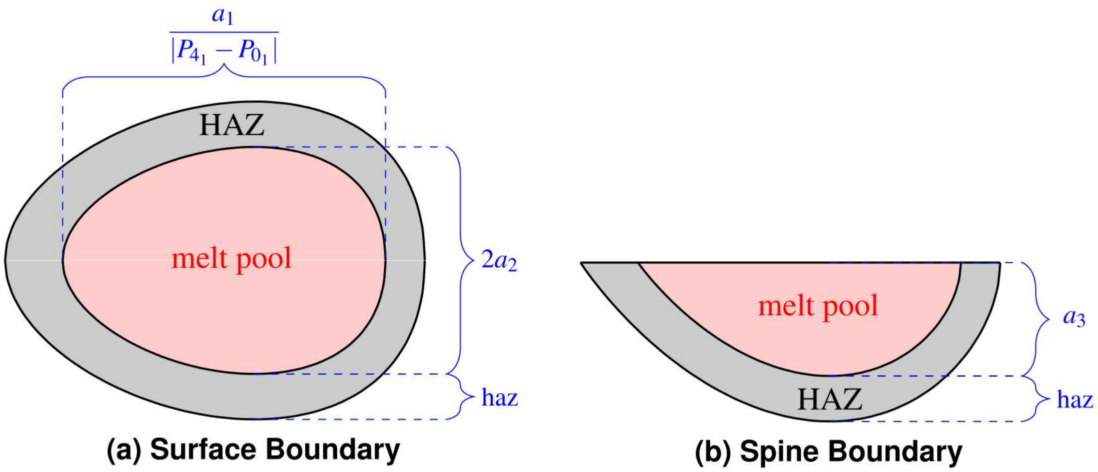

(a) Surface Boundary **(b) Spine Boundary**

Table 3-4. Nominal parameters values.

Parameter	Value
shape	case II
haz	30 sites
v_p	15 sites per MCS
a_1	100 sites
a_2	100 sites
a_3	80 sites

and III respectively. Probably the most striking difference between Figures 3-5, 3-6, and 3-7 are the tall columnar grains evident in both X- and Y-cuts where grains for Cases II and III extend across multiple layers. This is easily observed in Figures 3-5d, 3-5e, 3-7d, and 3-7e. Conversely, grains in Case I are significantly shorter and layers are clearly distinguishable in Figures 3-6d and 3-6e. In comparing Figures 3-7c, 3-5c, and 3-6c, we see Case III generates more regular structure than Case II which generates more regular structure than Case I. Longer pool shapes allow sites to spend more time in the HAZ allowing for additional grain growth – including epitaxial growth.

3.2.2. Variances in haz

In this section, the haz parameter is isolated and varied to help understand its effect on microstructure; all other parameters are held fixed to nominal values given in Table 3-4. In

Figure 3-5. Nominal base case generated microstructure.

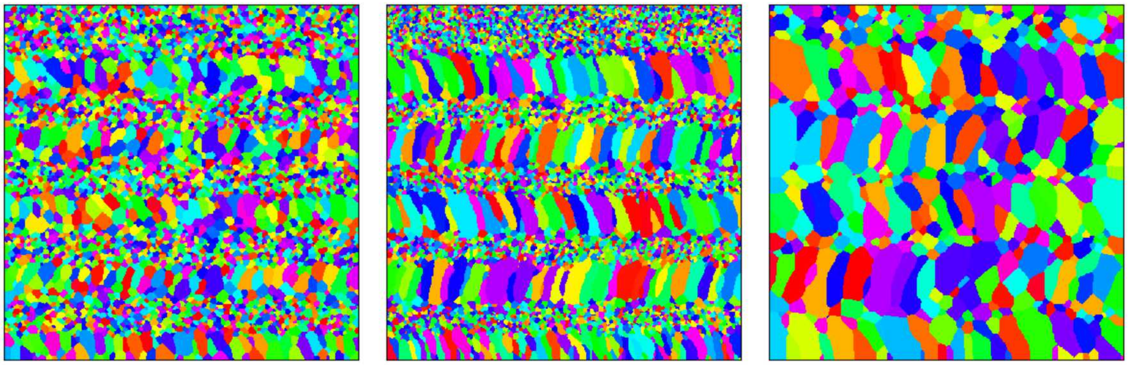

(a) $z = 1$ **(b)** $z = 64$ **first pass** **(c)** $z = 64$ **second pass**

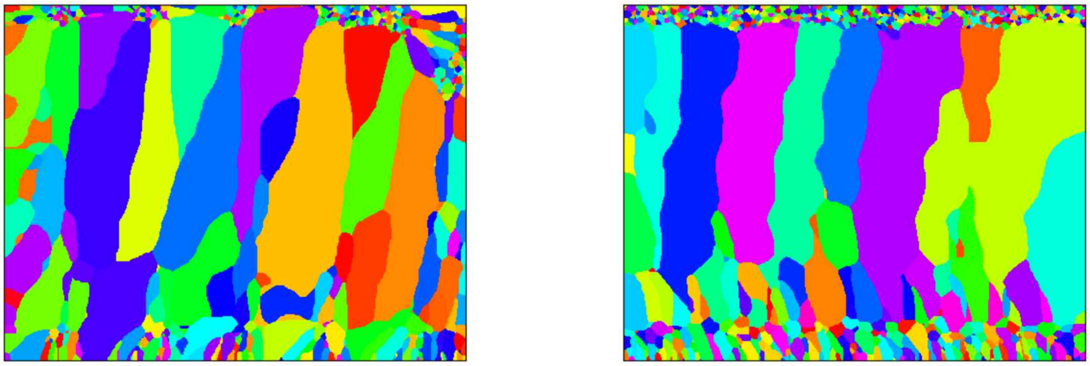

(d) $x = 250$ **(e)** $y = 250$

Figure 3-6. Case I generated microstructure.

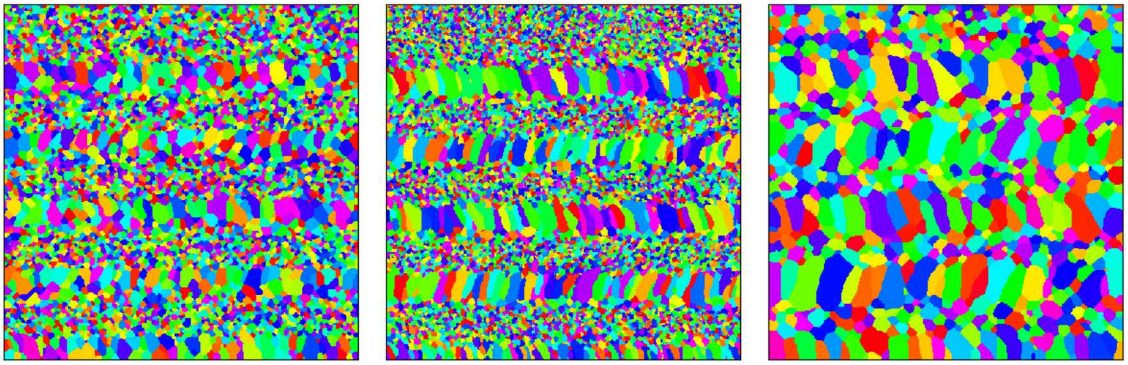

(a) $z = 1$ **(b)** $z = 64$ **first pass** **(c)** $z = 64$ **second pass**

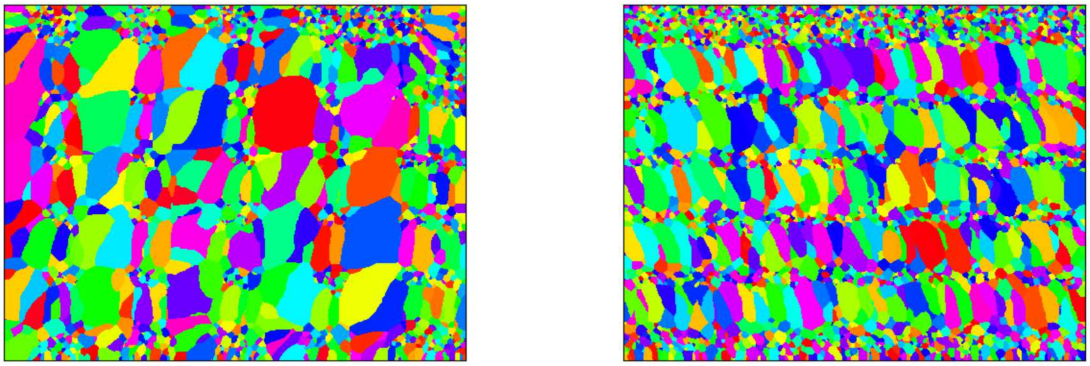

(d) $x = 250$ **(e)** $y = 250$

Figure 3-7. Case III generated microstructure.

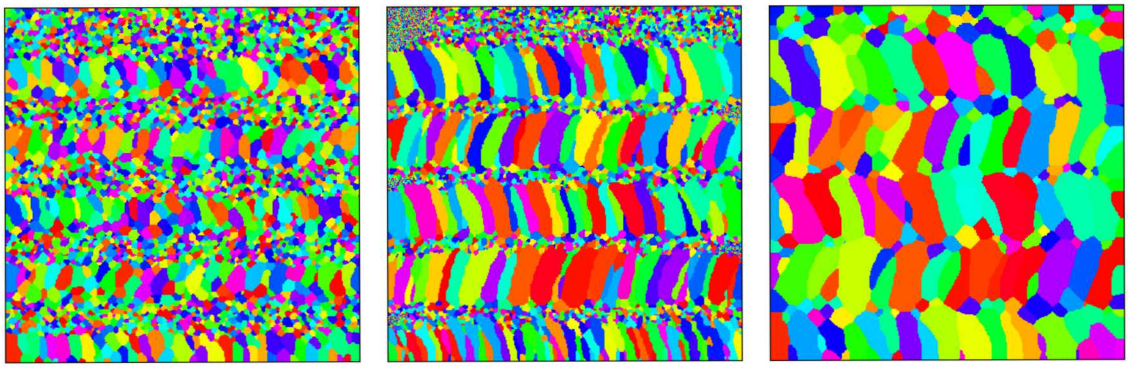

(a) $z = 1$ **(b)** $z = 64$ **first pass** **(c)** $z = 64$ **second pass**

(d) $x = 250$ **(e)** $y = 250$

Figure 3-8. haz $= 15$ generated microstructure.

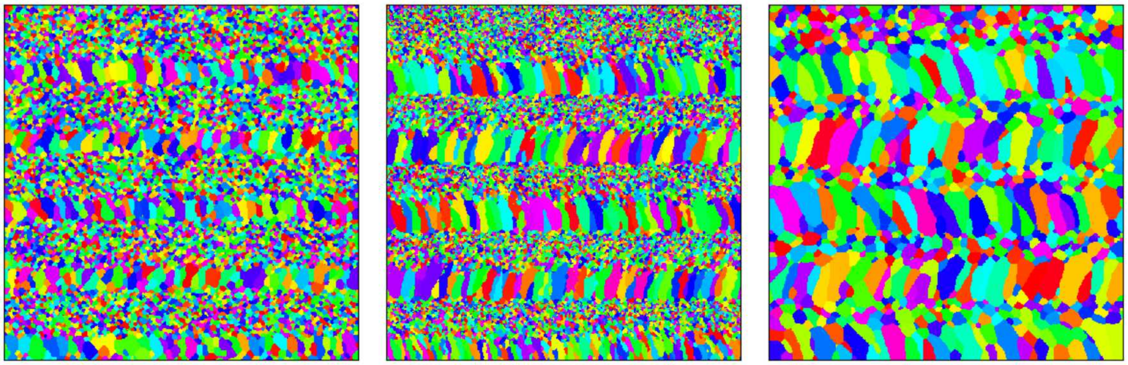

(a) $z = 1$ **(b)** $z = 64$ **first pass** **(c)** $z = 64$ **second pass**

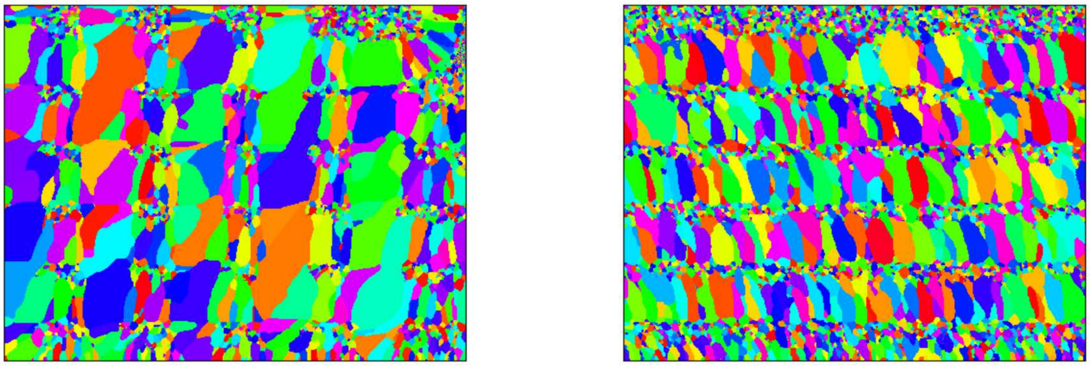

(d) $x = 250$ **(e)** $y = 250$

Figures 3-8 and 3-9 are microstructure images generated for an haz of 15 and 45 sites respectively. By comparing Figures 3-8 and 3-9 with Figure 3-5, we see that a larger haz of 45 sites creates very large columnar grains spanning multiple layers in the transverse X- and Y-cut images. Increasing the haz parameter enlarges the overall HAZ and generally encourages grain growth. These large columnar grains oriented along build axes are the result of epitaxial growth associated with multiple scan passes in combination with the larger HAZ. When the haz is 15 sites, we observe the opposite effect – relatively smaller grains in the transverse X and Y-cut images; layers are distinguishable in the transverse cuts; there is columnar growth but generally not across layer boundaries.

3.2.3. Variances in laser scan speed v_p

In this section we isolate and vary the parameter v_p from the nominal value of 15 sites per MCS listed in Table 3-4. Shown in Figures 3-10 and 3-11 are snapshots of microstructures generated by v_p selections of 12 and 18 sites per MCS respectively. It is clear from Figures 3-5, 3-10, and 3-11

Figure 3-9. haz $= 45$ **generated microstructure.**

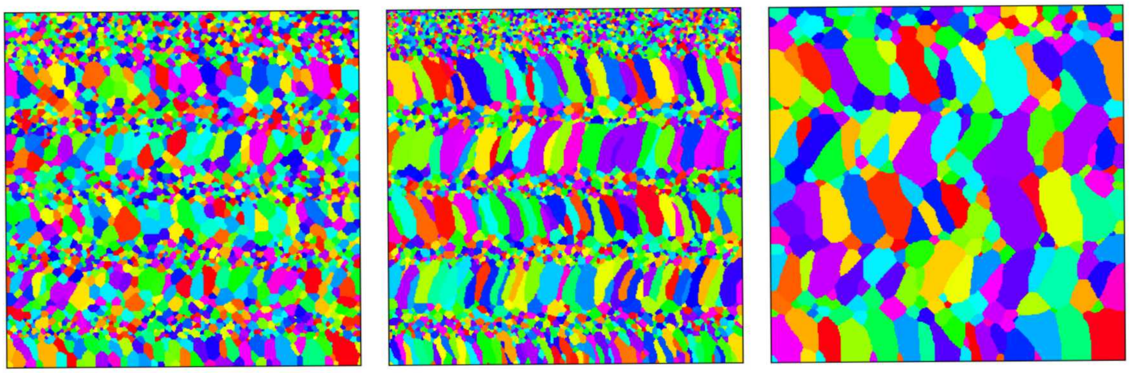

(a) $z = 1$ **(b)** $z = 64$ **first pass** **(c)** $z = 64$ **second pass**

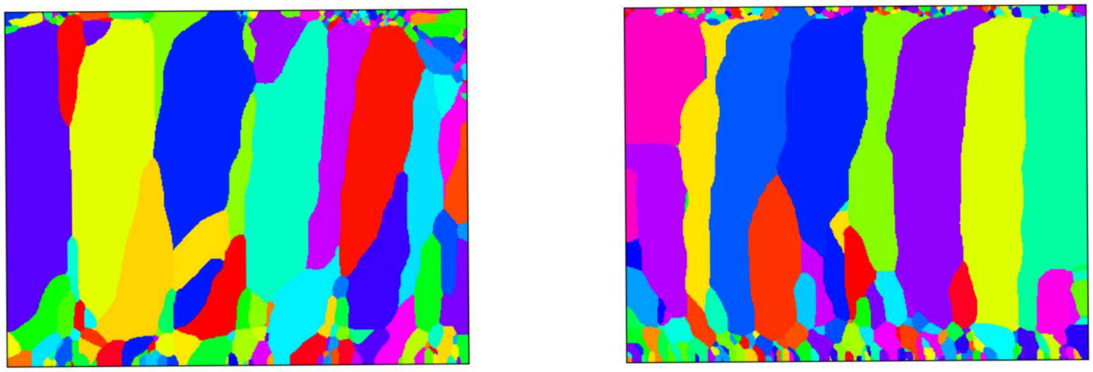

(d) $x = 250$ **(e)** $y = 250$

Figure 3-10. $v_p = 12$ **generated microstructure.**

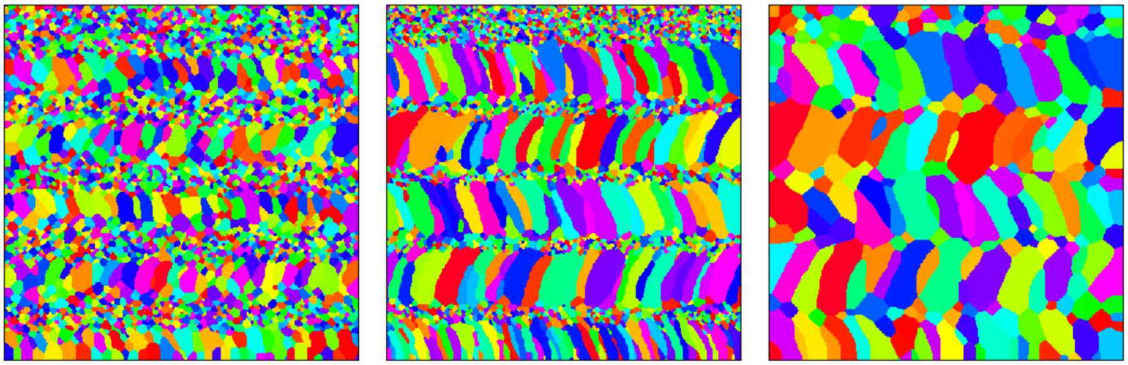

(a) $z = 1$ **(b)** $z = 64$ **first pass** **(c)** $z = 64$ **second pass**

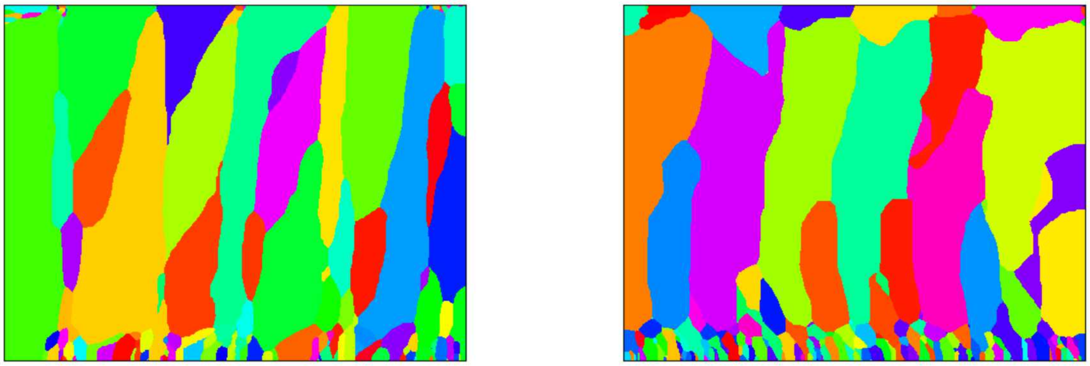

(d) $x = 250$ **(e)** $y = 250$

that higher speeds create microstructures with smaller grains; at any particular site, dwell time within the HAZ will generally be smaller at higher scan speeds. Lower dwell time provides less opportunity for grain growth resulting in smaller grains overall. For v_p selections of 12 and 15 sites per MCS shown in Figures 3-5 and 3-11, columnar grains are pronounced and cross layer boundaries in transverse X and Y-cut images.

3.2.4. Variances in melt pool depth a_3

In this section we isolate and vary the melt pool depth parameter a_3 from the nominal value of 80 sites listed in Table 3-4. Shown in Figure 3-12 and 3-13 are snapshots of microstructures generated for a_3 selections of 70 and 100 sites respectively. Interestingly, it appears smaller depths induce more grain growth and less grain nucleation. Intuitively this makes sense as the melt pool does not extend as far into the layer below and thus rather than melting, which allows grain nucleation, microstructure growth is generated by sites within the HAZ. Moreover, seen in

Figure 3-11. $v_p = 18$ **generated microstructure.**

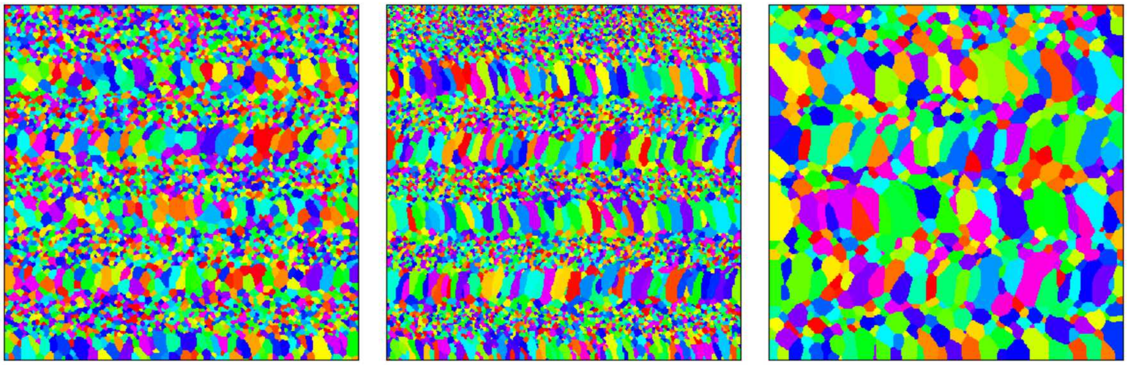

(a) $z = 1$ **(b)** $z = 64$ **first pass** **(c)** $z = 64$ **second pass**

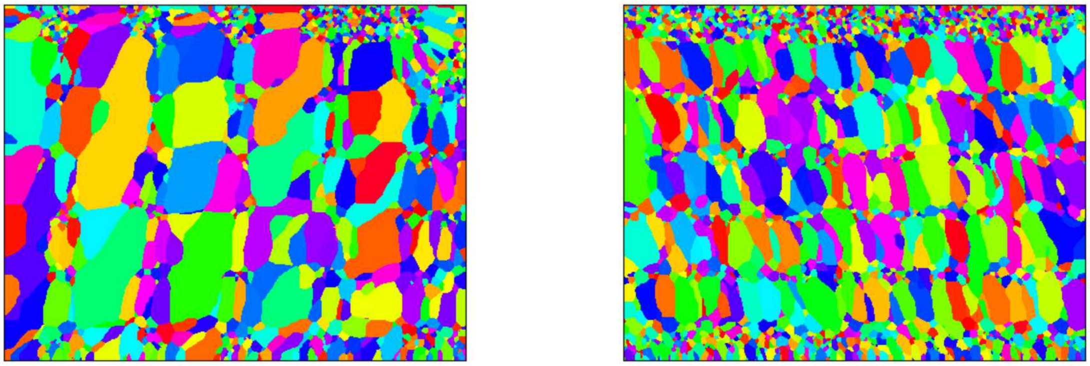

(d) $x = 250$ **(e)** $y = 250$

Figure 3-12. Depth $a_3 = 70$ generated microstructure.

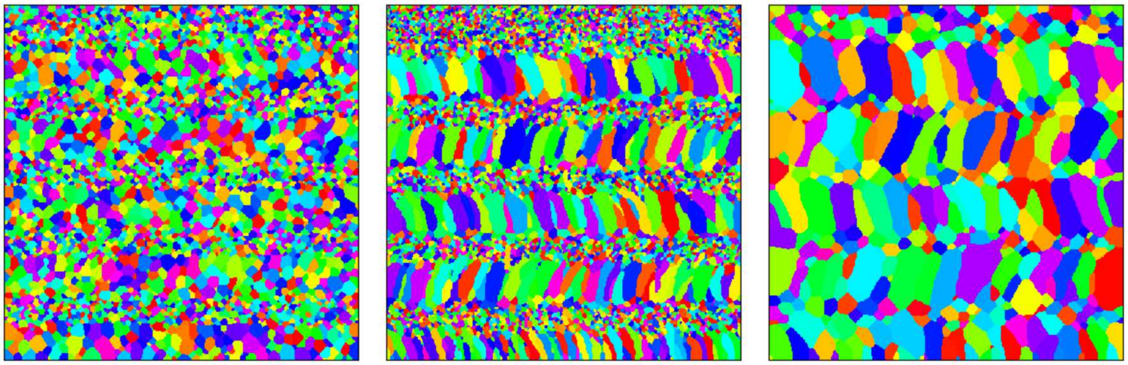

(a) $z = 1$ **(b)** $z = 64$ **first pass** **(c)** $z = 64$ **second pass**

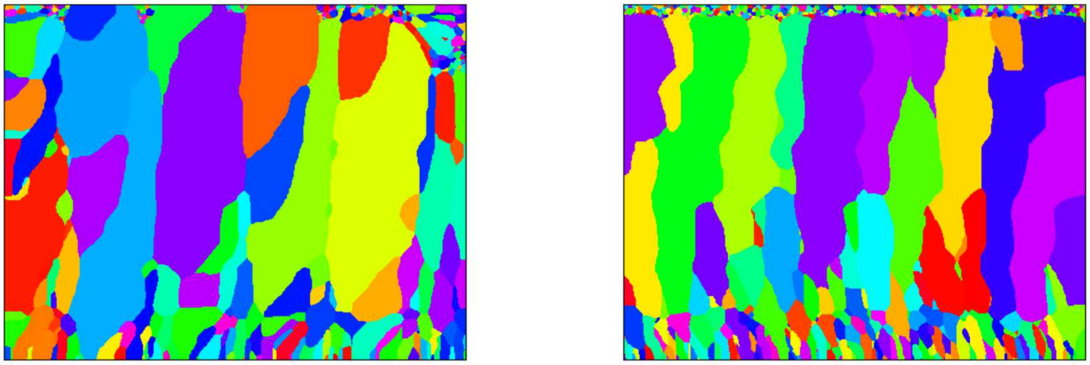

(d) $x = 250$ **(e)** $y = 250$

Figures 3-5c, 3-12c, and 3-13c, the increase in grain growth for a shallower melt pool is not restricted to the vertical direction, but rather extends into the horizontal as well.

3.2.5. Parameter experiments summary

In this section, exploratory parameter studies were conducted and presented. These studies include visual comparisons of process parameter effects on synthetically generated microstructures; parameters studied include laser scan speed, melt pool depth, and size of heat affected zone. Studies were also conducted on melt pool shapes ranging from nearly elliptical to teardrop.

This study was certainly not exhaustive but parameter variations did yield interesting effects on synthetically generated microstructures. Melt pool shape strongly influences microstructures; from X-cut visualizations we find that elongated pools tend to produce larger columnar type microstructures; for the most elliptical shape case I, columnar grains are predominantly confined

Figure 3-13. Depth $a_3 = 100$ generated microstructure.

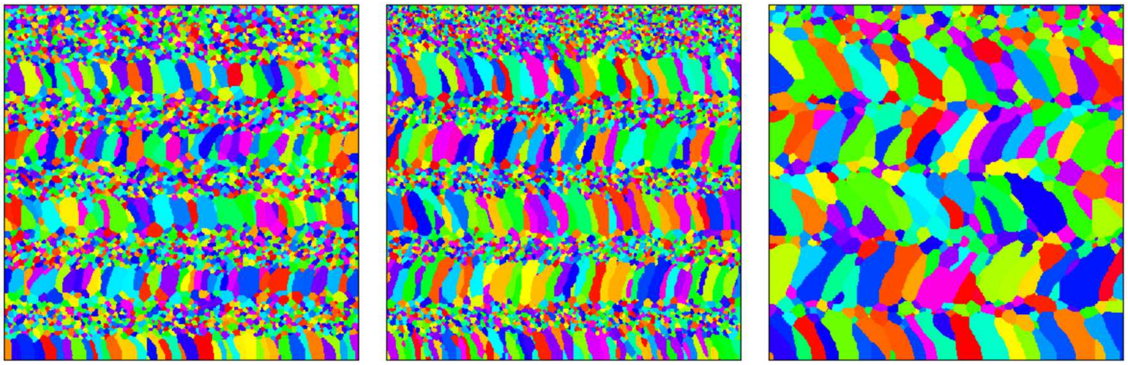

(a) $z = 1$ **(b)** $z = 64$ **first pass** **(c)** $z = 64$ **second pass**

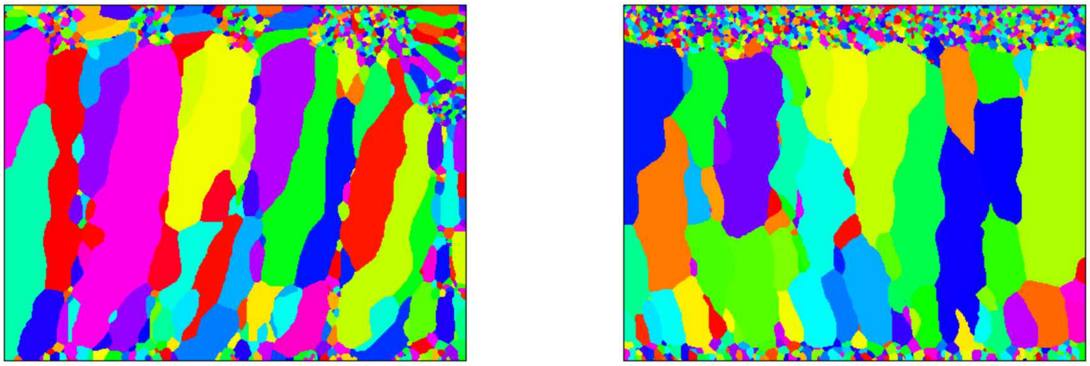

(d) $x = 250$ **(e)** $y = 250$

to a single layer whereas the highly-teardropped shape case III generates columnar structures spanning multiple layers. The haz parameter, which controls the size of the HAZ, also strongly influences columnar growth in X-cut visualizations where smaller values tend to confine columnar grains to a single layer whereas larger values produce columnar microstructures spanning multiple layers. Generally, slower laser scan speeds were found to produce larger columnar microstructures than faster laser scans.

Studies in this paper also illustrate evolution of microstructures on a layer due to melting and fusion effects from subsequent build layers. Melt pool depth is a significant factor which controls the degree of fusion of the current build layer with the previous layer. For the model presented in this paper, melt pool depth should be greater than one layer thickness to simulate melting, fusing, and solidifying of the current build layer with the previous layer. On the other hand, melt pool depths greater than two times layer thickness are possible but logically seem detrimental as melting material two layers below the current build layer is undesirable. Generally speaking, melt pool depth is nominally one and a half times layer thickness.

General observations regarding this model: smaller grains are generated by shortening the melt pool, reducing the HAZ region, increasing weld speed, or increasing melt pool depth.

4. CONCLUSIONS AND FUTURE WORK

In this paper a new model for simulating AM microstructures was presented. Bèzier curves were used to represent the melt pool surface arising from a laser heat source in the AM process; these differentiable curves are smooth and use control points to define specific melt pool geometry which allows for a great deal of flexibility in defining melt pool shapes. The model simulates melting, fusion, the heat affected zone, and evolution of microstructures associated with AM. The novel geometric formulation of our laser melt pool geometry has a great deal of flexibility. Three sets of control points were presented representing three melt pool shape examples ranging from somewhat elliptical to teardrop. The model has been implemented in the open source kinetic Monte Carlo framework SPPARKS. In this work we presented exploratory numerical studies on AM process parameters and melt pool shape to evaluate effects on synthetically generated microstructures. All simulations presented were done using SPPARKS.

There are a variety of additional features planned in future releases of the SPPARKS AM/Bézier application. Allowing more general melt pool geometries is a desirable property. Rather than selecting from three predefined geometries, we plan to allow control point selection for the two Bézier curves describing the melt pool surface and spine. This will enable a great deal of freedom towards selection of melt pool geometry. Another planned feature is the simulation of pulsed laser power; this is possible because of the novel melt pool geometry formulation in this work. We also plan parameter calibration and validation studies with microstructures observed from AM builds; this will help towards making this model and the SPPARKS application a production tool for the simulation of AM microstructures.

REFERENCES

[1] David P. Adams, Benjamin Reedlunn, Michael C. Maguire, Bo Song, Jay Carroll, Joseph E. Bishop, Jack L. Wise, Alice Kilgo, Todd Palmer, Don Brown, and Bjorn Clausen. Mechanical response of additively manufactured (AM) stainless steel 304L across a wide range of loading conditions. Technical Report SAND2019-7001, Sandia National Laboratories, 2019.

[2] M. P. Anderson, D. J. Srolovitz, G. S. Grest, and P. S. Sahni. Computer simulation of grain growth—I. kinetics. *Acta metallurgica*, 32(5):783–791, 1984.

[3] Anthony L. Garcia, Veena Tikare, and Elizabeth A. Holm. Three-dimensional simulation of grain growth in a thermal gradient with non-uniform grain boundary mobility. *Scripta Materialia*, 59(6):661 – 664, 2008.

[4] Elizabeth A. Holm and Corbett C. Battaile. The computer simulation of microstructural evolution. *Jom*, 53(9):20–23, 2001.

[5] John A. Mitchell and Veena Tikare. A model for grain growth during welding. Technical Report SAND2016-11070, Sandia National Laboratories, 2016.

[6] Steve Plimpton, Corbett Battaile, Mike Chandross, Liz Holm, Aidan Thompson, Veena Tikare, Greg Wagner, Ed Webb, Xiaowang Zhou, Garcia C. Cardona, and Alex Slepoy. Crossing the mesoscale no-man's land via parallel kinetic Monte Carlo. Technical Report SAND2009-6226, Sandia National Laboratories, 2009.

[7] Theron M. Rodgers, Jonathan D. Madison, and Veena Tikare. Simulation of metal additive manufacturing microstructures using kinetic Monte Carlo. *Computational Materials Science*, 135:78 – 89, 2017.

[8] Theron M. Rodgers, Jonathan D. Madison, Veena Tikare, and Michael C. Maguire. Predicting mesoscale microstructural evolution in electron beam welding. *JOM*, 68(5):1419–1426, 2016.

[9] Theron M. Rodgers, John A. Mitchell, and Veena Tikare. A Monte Carlo model for 3D grain evolution during welding. *Modelling and Simulation in Materials Science and Engineering*, 25(6):064006, aug 2017.

[10] Andrew M. Stine, Stanley W. Pierce, and Paul F. Moniz. Evaluation of Molybdenum as a Surrogate for Iridium in the GPHS Weld Development. Technical Report LA-UR-15-28088, Los Alamos National Laboratory, October 2015.

DISTRIBUTION

Hardcopy—External

Number of Copies	Name(s)	Company Name and Company Mailing Address

Hardcopy—Internal

Number of Copies	Name	Org.	Mailstop

Email—Internal (encrypt for OUO)

Name	Org.	Sandia Email Address
Technical Library	01177	libref@sandia.gov